ACS APPLIED MATERIALS & INTERFACES

Letter

www.acsami.org

Organic Solvent-Free, One-Step Engineering of Graphene-Based Magnetic-Responsive Hybrids Using Design of Experiment-Driven Mechanochemistry

Kuo-Ching Mei,[†] Yukuang Guo,[†] Jie Bai,[†] Pedro M. Costa,[†] Houmam Kafa,[†] Andrea Protti,[‡] Robert C. Hider,[†] and Khuloud T. Al-Jamal*[,†]

[†]Institute of Pharmaceutical Science, King's College London, Franklin-Wilkins Building, 150 Stamford Street, London SE1 9NH, United Kingdom

[‡]Cardiovascular Division, James Black Centre, King's College London British Heart Foundation Centre of Excellence, London SE5 9NU, United Kingdom

S *Supporting Information*

ABSTRACT: In this study, we propose an organic solvent-free, one-step mechanochemistry approach to engineer water-dispersible graphene oxide/superparamagnetic iron oxide (GO/SPIOs) hybrids, for biomedical applications. Although mechanochemistry has been proposed in the graphene field for applications such as drug loading, exfoliation or polymer-composite formation, this is the first study to report mechanochemistry for preparation of GO/SPIOs hybrids. The statistical design of experiment (DoE) was employed to control the process parameters. DoE has been used to control formulation processes of other types of nanomaterials. The implementation of DoE for controlling the formulation processes of graphene-based nanomaterials is, however, novel. DoE approach could be of advantage as one can tailor GO-based hybrids of predicted yields and compositions. Hybrids were characterized by TEM, AFM FT-IR, Raman spectroscopy, and TGA. The dose−response magnetic resonance (MR) properties were confirmed by MR imaging of phantoms. The biocompatibility of the hybrids with A549 and J774 cell lines was confirmed by the modified LDH assay.

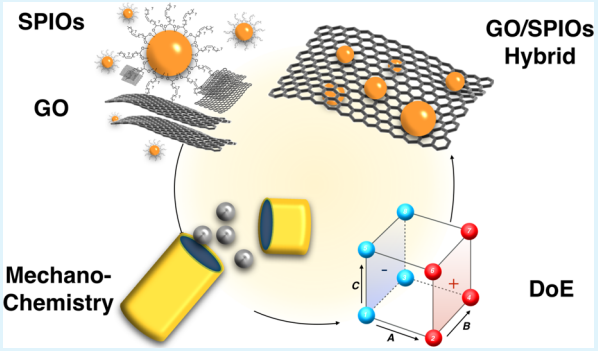

KEYWORDS: *graphene, mechanochemistry, DoE, SPIO, formulation, nanomedicine, drug delivery, toxicity*

Graphene is a single layer carbon sheet (~1 nm/layer) with sp^2 hybridization.[1] When oxidized to graphene oxide (GO), the material becomes water dispersible, which is a favorable property particularly in biomedicine. The nanometer-range dimension and large surface areas of GO provide great potential for targeted drug delivery and tissue engineering.[2,3] GO can also be covalently or noncovalently functionalized to provide additional features.[4] For example, GO hybridized with superparamagnetic iron oxide nanoparticles (SPIOs) has been reported as a theranostic platform (a single therapeutic and diagnostic system),[5] as a magnetic resonance imaging (MRI)/photoacoustic (PA) multimodal imaging system,[6] and as magnetically targeted nanocarriers capable of localized hyperthermia.[7]

Traditionally, the hybridization of GO with iron oxide nanoparticles has been reported using in situ synthesis,[8] direct graphitization of oleic acid coated iron oxide nanoparticles,[9] precipitation methods,[10−12] solvent-thermal method by autoclaving at 180 °C for 4−16 h,[13] direct mixing with heating at 98 °C,[14] and microwave-heated synthesis.[15] However, all of these methods involve the use of multistep processing,[8] organic solvents,[8,12−15] or external-heating.[8−10,13−15] An organic solvent-free, one-step process for formation of GO/SPIOs is still to be found. Mechanochemistry, however, has been proposed in the graphene field to exfoliate graphite with[16] or without drug loading,[17−21] to synthesize GO from graphite via oxidation reactions,[22,23] to functionalize graphene,[24−28] or to synthesize various graphene/graphite-polymer composites.[29−33] Mechanical force provides an alternative source of energy to control chemical reactivity that is usually achieved by thermal and chemical treatment.[34] Herein, we propose a one-step mechanochemistry approach to produce water-dispersible GO/SPIO hybrids, using a high-speed vibrational ball-mill. The process is deemed superior to previously reported methods, as it is simple and is organic solvent-free. Furthermore, no heating step is required. It is hypothesized in this study that the mechanical force, an alternative source to heat, can enhance the interaction between oleic acid coated SPIOs and GO, forming water-dispersible hybrids. In brief, freeze-dried GO and oleic acid coated hydrophobic SPIOs were loaded into the milling

Received: April 27, 2015
Accepted: June 23, 2015
Published: June 23, 2015

DOI: 10.1021/acsami.5b03577
ACS Appl. Mater. Interfaces 2015, 7, 14176−14181

jar, as dry powders, and dry milled for 1−2 h at 10−20 Hz. The control over the mechanical force and process parameters was achieved by implementation of the statistical design of experiment (DoE) (Figure 1A), as will be described later.

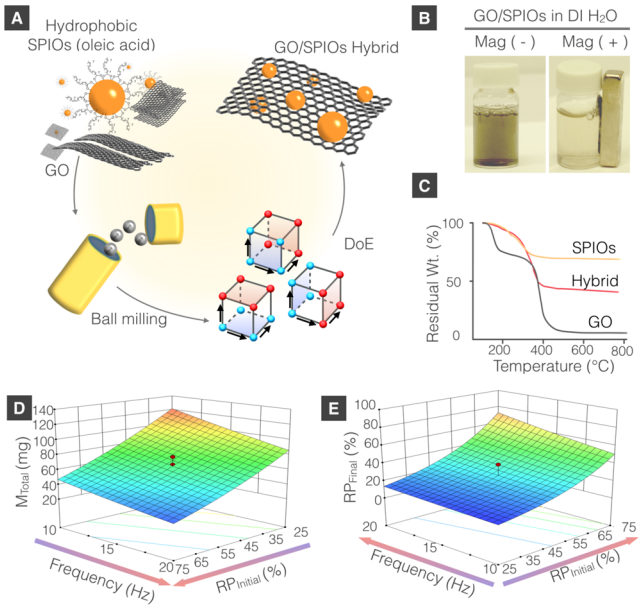

Figure 1. Engineering graphene-based magnetic responsive hybrids using mechanochemistry. (A) Schematic representation of GO/SPIO hybrid formulation. (B) Images of the water-dispersible GO/SPIO hybrid before and after exposure to a magnet (rated 0.42 T on its surface). (C) Representative thermogravimetric curves of GO, SPIOs, and GO/SPIO hybrid. The 3D response surface at center points (1.5 h) for (D) hybrid yield (M_{Total}) and (E) GO/SPIOs wt/wt % (RP_{Final}).

GO or SPIOs were milled alone as controls. Oleic acid coated SPIOs, milled in absence of GO remained hydrophobic and sedimented, from aqueous dispersions, upon standing. GO remained water-dispersible before and after ball milling and did not respond to the magnet. The water-dispersible hybrids were separated from hydrophobic SPIOs and GO, by leaving the dispersion to stand for 2 min, followed by magnetic separation, respectively, as described in the methods section. Figure 1B shows the black dispersion of ball-milled GO/SPIO hybrids, which turned transparent within 30 s of exposure to the magnet, indicating the magnetic responsiveness of the hybrid.

The total mass M_{Total} (SPIOs + GO) (mg) and the composition of the hybrid i.e. the final relative weight percentage of GO/SPIOs (RP_{Final}) were measured by thermogravimetric analysis (TGA). As illustrated in Figure 1C, GO decomposes completely at 800 °C, in compressed air. Oleic acid coated SPIOs demonstrated a weight loss of 31.48 ± 0.01% at 800 °C (n = 3), due to oleic acid combustion. Ball-milled GO/SPIO hybrids, however, showed a weight loss of 34−69% at 800 °C, indicating the presence of GO and SPIOs in the sample.

DoE constitutes an efficient procedure for planning experiments.[35] It offers the advantage of being able to investigate the effect of two or more factors, on a system, while keeping the number of runs minimal. As a result, DoE offers advantages of obtaining the same amount of information while keeping the number of experimental conditions minimal, without losing precision. A full 2-level factorial DoE can investigate the effect of three factors, i.e., variables, 2-factor interactions (2FI), and 3-factor interactions (3FI) on the responses, from only 8 experiments. Implementation of DoE for controlling the formulation processes of other types of nanocarriers such as liposomes,[36−38] nanosuspension,[39] and solid lipid nanoparticle[40] have been reported. There are no studies, however, which have employed this approach in processing graphene-based nanomaterials. To better understand the impact of formulation and process parameters, on GO/SPIO hybrid system formulation, DoE with a 2^3 (2-level 3 factors) full factorial design with replicated center points was introduced.[41] Three factors were included in the design: milling frequency in Hz (A), milling time in h (B), and the initial relative weight percentage of GO/SPIOs ($RP_{Initial}$), being loaded into the milling jar (C). Actual values of each factor were represented in coded pattern, i.e., +1 (high level) and −1 (low level) (Table S1 in the Supporting Information). Responses include the total weight of the hybrids in mg (M_{Total}) and RP_{Final}. M_{Total} represents the yield whereas RP_{Final} reflects the content of SPIOs within the hybrid. The design layout and response values are summarized in Table 1.

Table 1. Full Two-Level, Three-Factor Factorial Design

	factor			response	
std	A^a (Hz)	B^b (h)	C^c (%)	$M_{Total}{}^d$ (mg)	$RP_{Final}{}^e$ (%)
1	10	1	25	107.10	9.77
2	20	1	25	77.53	10.41
3	10	2	25	125.71	8.63
4	20	2	25	95.83	14.04
5	10	1	75	44.50	32.60
6	20	1	75	20.46	61.42
7	10	2	75	50.15	62.64
8	20	2	75	26.82	81.74
9	15	1.5	50	66.98	24.16
10	15	1.5	50	64.13	38.82
11	15	1.5	50	77.19	25.94

[a]Milling frequency in Hz. [b]Milling time in h. [c]Initial GO/SPIOs wt/wt %. [d]Total hybrid weight in mg. [e]Final GO/SPIOs wt/wt % in the hybrid.

The effect of factors, 2FI and 3FI on M_{Total} and RP_{Final} were calculated using eq S1 (Figure S1 and Table S2 in the Supporting Information). Detailed information on the effect evaluations and the establishment of predictive equations are described in the Supporting Information, methods and Figures S2−S5.

The final fitted model for the M_{Total} with the coded factors of milling frequency (A), milling time (B), and $RP_{Initial}$ (C) is shown in eq 1. A good correlation was obtained between the observed and predicted values as indicated by the R^2 value of 0.9795, adjusted R^2 value of 0.9707 and predicted R^2 value of 0.9578. In brief, milling frequency, milling time and the $RP_{Initial}$ significantly influenced the response M_{Total} (p-value <0.05). $RP_{Initial}$ (C) was the dominating factor toward M_{Total}, as it exhibited the largest coefficient compared to A and B. Higher milling frequency (A) and higher $RP_{Initial}$ (C) resulted in a lower M_{Total}, as indicated by their negative coefficients. Longer milling time (B), however, increased M_{Total}, as indicated by its positive coefficient. The predictive equation of coded and actual factors is represented in eq 2. A comparison of the predicted and actual (experimental) values for M_{Total} is shown in Figure S3 in the Supporting Information. A 3D factorial response

DOI: 10.1021/acsami.5b03577
ACS Appl. Mater. Interfaces 2015, 7, 14176−14181

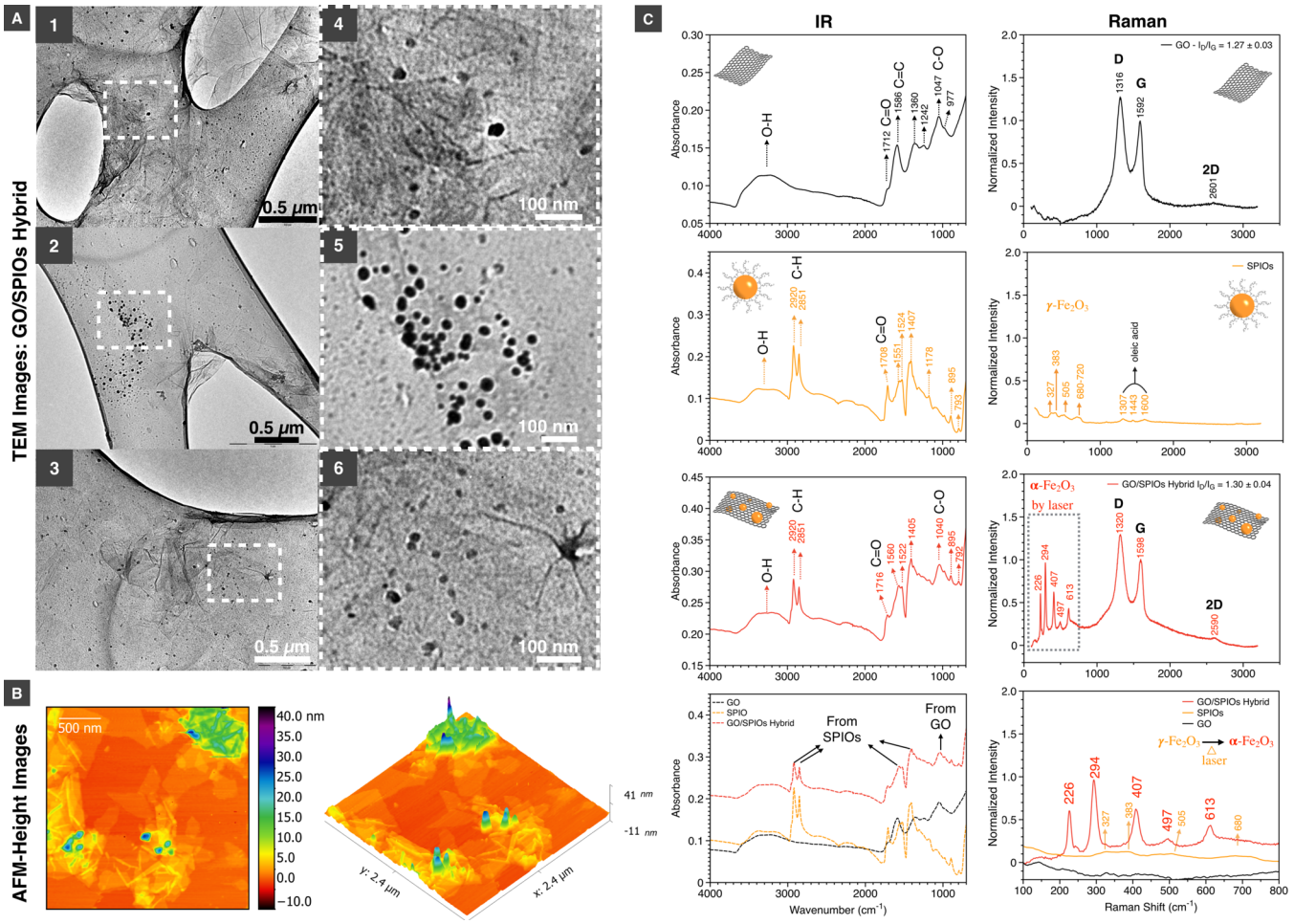

Figure 2. Characterization of GO/SPIOs hybrid. (A 1−3) TEM images of GO/SPIO hybrids on lacey carbon supports are shown. SPIOs were found as scattered black spots due to their higher electron density. (A 4−6) The 4× magnification of selected areas from A 1−3. (B) 2D and 3D AFM height images are shown. The height of the SPIOs is around 10−20 nm. (C) IR and Raman spectra of starting materials and the hybrid.

surface was produced for M_{Total} according to the predictive eqs 1 and 2 and is shown in Figure 1D.

$$\sqrt{M_{Total}} = 8.05 - 0.88A + 0.36B - 2.09C \quad (1)$$

$$\sqrt{M_{Total}} = 13.77 - 0.18\text{Frequency(HZ)} + 0.73\text{Time (h)} - 0.08\text{RP}_{Initial}\ (\text{wt/wt\%}) \quad (2)$$

The final fitted model for the RP_{Final} with the coded factors of milling frequency (A), milling time (B), and $RP_{Initial}$ (C) is shown in eq 3. A good correlation was obtained between the observed and predicted values as indicated by the R^2 value of 0.9438, adjusted R^2 value of 0.9197 and predicted R^2 value of 0.8662. In brief, higher milling frequency, higher $RP_{Initial}$ and longer milling time all resulted in a higher RP_{Final} as reflected by their positive coefficient. The predictive equation of coded and actual factors is represented in eq 4. A comparison of the predicted and actual (experimental) values for RP_{Final} is shown in Figure S5 in the Supporting Information. A 3D factorial response surface was produced for RP_{Final} according to the predictive eqs 3 and 4 and is shown in Figure 1E.

$$\log \text{RP}_{Final} = 1.41 + 0.08A + 0.06B + 0.37C \quad (3)$$

$$\log \text{RP}_{Final} = 0.26 + 0.02\text{Frequency (Hz)} + 0.12\text{Time (h)} + 0.01\text{RP}_{Initial}\ (\text{wt/wt\%}) \quad (4)$$

Using DoE, it was established that a higher initial SPIOs loading, i.e., lower $RP_{Initial}$ value, and longer milling time resulted in hybrids of higher SPIOs content, i.e., lower RP_{Final} value (Figure 1E). Higher milling frequency adversely affected both M_{Total} and SPIOs content in the hybrids (Figure 1D, E). From these studies, it was concluded that the DoE approach could be reliably implemented in the process of formulating GO-SPIOs hybrids.

Morphological examination of GO and GO/SPIO hybrids was performed using transmission electron microscopy (TEM) and atomic force microscopy (AFM). The TEM and AFM images of GO sheets are shown in Figures S6 and S7 in the Supportng Information, respectively. The height of the GO sheets, as shown with AFM, is ∼1 nm confirming the formation of single-layer GO sheets. The size (surface area) of GO was generally small, with a medium area of 181.35 nm^2 and an average of 441 nm^2 (n = 438) (Figure S7 in the Supporting Information). TEM images of the GO/SPIO hybrids showed electron-dense structures, typical of SPIOs, associated with GO sheets confirming the formation of GO/SPIO hybrids (Figure 2A). AFM images showed height between 10 and 20 nm, which agreed with the theoretical size of the SPIOs (Figure 2B and

DOI: 10.1021/acsami.5b03577
ACS Appl. Mater. Interfaces 2015, 7, 14176−14181

Figure S8 in the Supporting Information). Some larger SPIOs aggregates could be also found (Figure S9 in the Supporting Information). This was expected as the milling processing occurred under dry conditions. The breaking of the SPIOs aggregates is dependent on the process-capability of the ball-mill, which is one of the limitations of this approach.

In our study, stabilization of GO-SPIOs hybrids, upon ball-milling, could be a result of enhanced hydrophobic or $\pi-\pi$ interactions between the oleic acid coated SPIOs and aromatic rings of GO. Alternatively, GO's oxygen-containing functional groups, i.e., COOH could interact with SPIOs, mimicking the ligand exchange process. Mechanical force has been reported to exchange the ligand on oleic acid coated iron oxide nanoparticles with poly(acrylic acid), polyethylenimine, and glutathione.[42] A slight to moderate increase in temperatures inside the milling jar may have occurred. Temperatures, however, remained lower (<40 °C) than those reported in previous studies (>95 °C), used to formulate GO/SPIOs hybrids.[8−10,13,14] Avoiding high-temperature is of critical importance when conjugating biomolecules i.e., targeting peptides or antibodies.

IR and Raman spectra of GO, SPIOs and the hybrids are shown in Figure 2C. The C−H stretching vibrations, at 2920 and 2851 cm^{-1}, corresponding to the oleic acid coating can be seen in both SPIOs and GO/SPIOs. The presence of oleic acid in GO/SPIO hybrids may have facilitated flocculation overtime (Figure 1B, left panel). Future work could involve PEGylation of GO/SPIO hybrid to improve physical stability. Characteristic D and G bands can be seen in GO and GO/SPIOs hybrids with I_D/I_G peak-height ratios of 1.30 ± 0.04 and 1.27 ± 0.04, respectively ($p > 0.05$, $n = 3$). Both IR and Raman spectra confirmed the formation of the hybrid. In addition to mechanical forces, it is anticipated that the mild milling may result in local heat generation, at the nanointerface, which is required to enhance hydrophobic or $\pi-\pi$ interactions forming the hybrid. The weak but characteristic Raman peaks of γ-Fe_2O_3 (maghemite) can be seen at 327, 383, 505, and 680−720 cm^{-1} (Figure 2C Raman spectra). Under the same laser power (1%), these peaks were difficult to be visualized in GO/SPIOs hybrids, as shown in Figure S10 in the Supporting Information.

When samples were preheated with higher power laser (50%) during Raman measurement, the appearance of 5 peaks, characteristic of α-Fe_2O_3 at 226, 294, 407, 497, 613 cm^{-1}, could be seen in GO/SPIO hybrids (Figure 2C and the Raman spectra in FIgure S10 in the Supporting Information). It is known that Fe_3O_4 and γ-Fe_2O_3 (maghemite) can undergo phase-transformation to α-Fe_2O_3 (hematite), which exhibits different Raman spectrum. This transformation can be artificially triggered when heated by laser.[43] Raman spectroscopy did not only confirm the formation of the hybrid but also suggested that if heat was generated during the milling process, then the amount produced was not sufficient to induce transformation of γ-Fe_2O_3 to α-Fe_2O_3. The Raman spectra of SPIOs and GO/SPIO hybrids measured using different laser power are shown in Figure S-10.

In vitro toxicity of the GO/SPIO hybrids was also evaluated using A549 cells (adenocarcinoma human alveolar basal epithelial cells) and J774 cells (murine macrophages). Optical microscopy images of A549 and J774 cells, incubated with GO/SPIO hybrids, were captured after 24 and 72 h. GO/SPIO hybrids are expressed based on SPIOs concentration. Cells incubated with GO/SPIO hybrids showed normal morphology at all concentrations tested while cells treated with dimethyl sulfoxide (DMSO), used as a positive control, appeared unhealthy and detached from the plate. The extent of GO/SPIO hybrids taken up by cells was concentration- and time-dependent (Figure S11 in the Supporting Information).

The modified lactate dehydrogenase (mLDH) assay was used to assess the cytotoxicity of GO/SPIO hybrids on A549 cells and J774 cells using the method described in the methods in the Supporting Information.[44] Cells were incubated with the hybrids at 10, 25, 50, and 100 μg/mL for 24 and 72 h. DMSO resulted in viability of 2.2% and 1.80% for A549 and J774 cells, respectively. The cytotoxicity result from the mLDH assay is shown in Figure 3. No statistically significant effect on cell viability was observed in all treated groups up to 100 μg/mL for 72 h. Reported studies in the literature showed no significant toxicity for SPIOs or GO up to 100 μg/mL.[45,46]

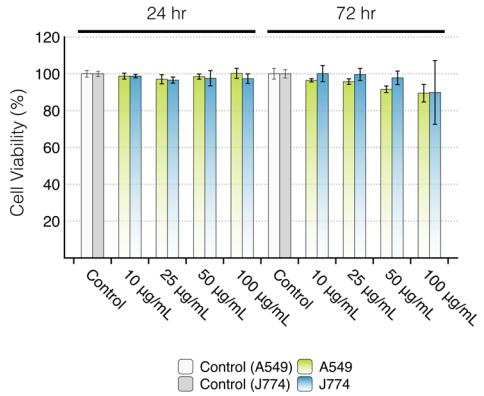

Figure 3. Modified LDH assay of A549 and J774 cells incubated with GO/SPIO hybrids. The A549 and J774 cells were incubated with GO/SPIO hybrids at SPIOs concentrations of 10, 25, 50, and 100 μg/mL for 24 and 72 h. The toxicity was assessed using the modified LDH assay. No significant effect on cell viability was observed.

To demonstrate the imaging potential of the GO-SPIOs hybrids, their MR contrast properties were determined by an in vitro MR phantom study using a 7T MR scanner. The GO/SPIOs hybrid samples were suspended in 1% agarose to mimic the tissue-like environment in vivo.[47] Their transverse (T_2) relaxation times were measured at increasing Fe concentrations and the R_2 ($1/T_2$) values were calculated. The GO/SPIOs hybrids exhibited a concentration-dependent darkening effect with an r_2 relaxivity of 144 mMs^{-1} (Figure 4A, B). The

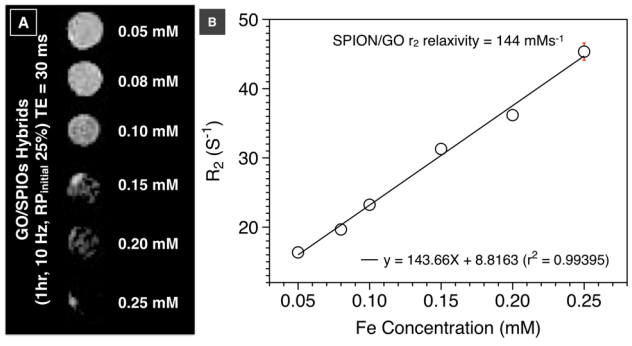

Figure 4. Phantom MR imaging of GO/SPIO hybrids. (A) T_2-weighted phantom MR imaging of GO/SPIO hybrids at increasing Fe concentrations. (B) R_2 relaxation rate analysis as a function of Fe concentration.

DOI: 10.1021/acsami.5b03577
ACS Appl. Mater. Interfaces 2015, 7, 14176−14181

obtained values are higher than some of those GO-based MRI imaging nanocomposites reported in literature.[7,48] The obtained r_2 relaxivity was comparable to values reported for the commercially approved MRI contrast agent Feridex (127.47 and 108 mM s^{-1})[49,50] Regional signal reductions were seen with the GO/SPIO hybrids and became more obvious at higher Fe concentrations. The heterogeneous hypointense signals are likely to be due to the inhomogeneous presence of iron oxide in the hybrids as observed in TEM and AFM images. The T_2-weighted contrast enhancement, combined with water-dispersibility, made the GO-SPIOs as a potential MR imaging agent in the future.

In conclusion, engineering GO/SPIO hybrids using organic solvent-free mechanochemistry is reported for the first time. The mechanochemistry approach replaced the traditional solvent-based and/or external heat-based treatment for GO/SPIO hybridization. The formulation process was rendered eco-friendly, i.e., organic solvent-free without significant heating being produced, as confirmed by Raman spectroscopy. The preparation time was dramatically reduced to a maximum of 1−2 h. The purification step is rapid, simple and only requires a magnet. The resulting GO/SPIO hybrids showed no significant toxicity on A549 and J774 cells at the SPIOs concentrations up to 100 μg/mL and 72 h. Hybrids produced were water-dispersible and showed dose-dependent MR properties. The mechanochemical approach was combined with the DoE, which has been used for the first time, to design GO-based hybrids of predicted yields and compositions. Simple preparative methods combined with predicted design of hybrid nanomaterial provides the foundation for future applications with quality by design (QbD), which is important for clinically relevant materials.[51] This approach could be extended to prepare other types of nanohybrids after careful consideration.

■ ASSOCIATED CONTENT

Supporting Information

Experiment materials, methods, and additional figures. The Supporting Information is available free of charge on the ACS Publications website at DOI: 10.1021/acsami.5b03577.

■ AUTHOR INFORMATION

Corresponding Author

*E-mail: khuloud.al-jamal@kcl.ac.uk.

Notes

The authors declare no competing financial interest.

■ ACKNOWLEDGMENTS

K.C.M. thanks King's College London for the Graduate School International Research Award (GSIRA) studentship. Funding from Biotechnology and Biological Sciences Research Council (BB/J008656/1) and FP7-ITN Marie-Curie Network program RADDEL (290023) are acknowledged. J.B. is sponsored by the China Scholarship Council (CSC)-King's PhD award. H.K. is sponsored by the Atomic Energy Commission of Syria. P.M.C. is a Sir Henry Wellcome Postdoctoral fellow (WT103913).

■ REFERENCES

(1) Novoselov, K. S. Nobel Lecture: Graphene: Materials in the Flatland. *Rev. Mod. Phys.* **2011**, *83*, 837−849.

(2) Yang, K.; Zhang, S.; Zhang, G.; Sun, X.; Lee, S.-T.; Liu, Z. Graphene in Mice: Ultrahigh in Vivo Tumor Uptake and Efficient Photothermal Therapy. *Nano Lett.* **2010**, *10*, 3318−3323.

(3) Zhang, Y.; Nayak, T. R.; Hong, H.; Cai, W. Graphene: a Versatile Nanoplatform for Biomedical Applications. *Nanoscale* **2012**, *4*, 3833−3842.

(4) Georgakilas, V.; Otyepka, M.; Bourlinos, A. B.; Chandra, V.; Kim, N.; Kemp, K. C.; Hobza, P.; Zboril, R.; Kim, K. S. Functionalization of Graphene: Covalent and Non-Covalent Approaches, Derivatives and Applications. *Chem. Rev.* **2012**, *112*, 6156−6214.

(5) Yang, K.; Feng, L.; Shi, X.; Liu, Z. Nano-Graphene in Biomedicine: Theranostic Applications. *Chem. Soc. Rev.* **2013**, *42*, 530−547.

(6) Yang, K.; Hu, L.; Ma, X.; Ye, S.; Cheng, L.; Shi, X.; Li, C.; Li, Y.; Liu, Z. Multimodal Imaging Guided Photothermal Therapy Using Functionalized Graphene Nanosheets Anchored with Magnetic Nanoparticles. *Adv. Mater.* **2012**, *24*, 1868−1872.

(7) Ma, X.; Tao, H.; Yang, K.; Feng, L.; Cheng, L.; Shi, X.; Li, Y.; Guo, L.; Liu, Z. A Functionalized Graphene Oxide-Iron Oxide Nanocomposite for Magnetically Targeted Drug Delivery, Photothermal Therapy, and Magnetic Resonance Imaging. *Nano Res.* **2012**, *5*, 199−212.

(8) Singh, V. K.; Patra, M. K.; Manoth, M.; Gowd, G. S.; Vadera, S. R.; Kumar, N. In Situ Synthesis of Graphene Oxide and Its Composites with Iron Oxide. *New Carbon Materials* **2009**, *24*, 147−152.

(9) Mendes, R. G.; Bachmatiuk, A.; El-Gendy, A. A.; Melkhanova, S.; Klingeler, R.; Büchner, B.; Rümmeli, M. H. A Facile Route to Coat Iron Oxide Nanoparticles with Few-Layer Graphene. *J. Phys. Chem. C* **2012**, *116*, 23749−23756.

(10) Yang, X.; Chen, C.; Li, J.; Zhao, G.; Ren, X.; Wang, X. Graphene Oxide-Iron Oxide and Reduced Graphene Oxide-Iron Oxide Hybrid Materials for the Removal of Organic and Inorganic Pollutants. *RSC Adv.* **2012**, *2*, 8821−8826.

(11) Zubir, N. A.; Yacou, C.; Motuzas, J.; Zhang, X.; Diniz da Costa, J. C. Structural and Functional Investigation of Graphene Oxide−Fe3O4 Nanocomposites for the Heterogeneous Fenton-Like Reaction. *Sci. Rep.* **2014**, *4*.

(12) Lin, J.; Raji, A.-R. O.; Nan, K.; Peng, Z.; Yan, Z.; Samuel, E. L. G.; Natelson, D.; Tour, J. M. Iron Oxide Nanoparticle and Graphene Nanoribbon Composite as an Anode Material for High-Performance Li-Ion Batteries. *Adv. Funct. Mater.* **2013**, *24*, 2044−2048.

(13) Qian, W.; Chen, Z.; Cottingham, S.; Merrill, W. A.; Swartz, N. A.; Goforth, A. M.; Clare, T. L.; Jiao, J. Surfactant-Free Hybridization of Transition Metal Oxidenanoparticles with Conductive Graphene for High-Performance Supercapacitor. *Green Chem.* **2012**, *14*, 371−377.

(14) Guoxin, H.; Xu, Z. Monodisperse Iron Oxide Nanoparticle-Reduced Graphene Oxide Composites Formed by Self-Assembly in Aqueous Phase. *Fullerenes, Nanotubes and Carbon Nanostructures* **2014**, *23*, 283−289.

(15) Gollavelli, G.; Ling, Y.-C. Biomaterials. *Biomaterials* **2012**, *33*, 2532−2545.

(16) Rubio, N.; Serra-Maia, R.; Kafa, H.; Mei, K.-C.; Al-Jamal, K. T.; Luckhurst, W.; Zloh, M.; Festy, F.; Richardson, J. P.; Naglik, J. R.; Pach, E.; Ballesteros, B. Production of Water-Soluble Few-Layer Graphene Mesosheets by Dry Milling with Hydrophobic Drug. *Langmuir* **2014**, *30*, 14999−15008.

(17) Antisari, M.; Montone, A.; Jovic, N.; Piscopiello, E.; Alvani, C.; PilloniI, L. Low Energy Pure Shear Milling: a Method for the Preparation of Graphite Nano-Sheets. *Scripta Materialia* **2006**, *55*, 1047−1050.

(18) Zhao, W.; Fang, M.; Wu, F.; Wu, H.; Wang, L.; Chen, G. Preparation of Graphene by Exfoliation of Graphite Using Wet Ball Milling. *J. Mater. Chem.* **2010**, *20*, 5817−5819.

(19) Knieke, C.; Berger, A.; Voigt, M.; Taylor, R. N. K.; Röhrl, J.; Peukert, W. Scalable Production of Graphene Sheets by Mechanical Delamination. *Carbon* **2010**, *48*, 3196−3204.

(20) León, V.; Quintana, M.; Herrero, M. A.; Fierro, J. L. G.; Hoz, A.; de, L.; Prato, M.; Vázquez, E. Few-Layer Graphenes From Ball-Milling of Graphite with Melamine. *Chem. Commun.* **2011**, *47*, 10936−10938.

DOI: 10.1021/acsami.5b03577
ACS Appl. Mater. Interfaces 2015, 7, 14176−14181

(21) Yao, Y.; Lin, Z.; Li, Z.; Song, X.; Moon, K.-S.; Wong, C.-P. Large-Scale Production of Two-Dimensional Nanosheets. *J. Mater. Chem.* **2012**, *22*, 13494−13499.
(22) Posudievsky, O. Y.; Khazieieva, O. A.; Koshechko, V. G.; Pokhodenko, V. D. Preparation of Graphene Oxide by Solvent-Free Mechanochemical Oxidation of Graphite. *J. Mater. Chem.* **2012**, *22*, 12465−12467.
(23) Posudievsky, O. Y.; Kozarenko, O. A.; Khazieieva, O. A.; Koshechko, V. G.; Pokhodenko, V. D. Ultrasound-Free Preparation of Graphene Oxide From Mechanochemically Oxidized Graphite. *J. Mater. Chem. A* **2013**, *1*, 6658−6663.
(24) Yan, L.; Lin, M.; Zeng, C.; Chen, Z.; Zhang, S.; Zhao, X.; Wu, A.; Wang, Y.; Dai, L.; Qu, J.; Guo, M.; Liu, Y. Electroactive and Biocompatible Hydroxyl- Functionalized Graphene by Ball Milling. *J. Mater. Chem.* **2012**, *22*, 8367−8371.
(25) Jeon, I. Y.; Shin, Y. R.; Sohn, G. J.; Choi, H. J.; Bae, S. Y.; Mahmood, J.; Jung, S. M.; Seo, J. M.; Kim, M. J.; Wook Chang, D.; Dai, L.; Baek, J. B. Edge-Carboxylated Graphene Nanosheets via Ball Milling. *Proc. Natl. Acad. Sci. U.S.A.* **2012**, *109*, 5588−5593.
(26) Seo, J.-M.; Jeon, I.-Y.; Baek, J.-B. Mechanochemically Driven Solid-State Diels−Alder Reaction of Graphite Into Graphene Nanoplatelets. *Chem. Sci.* **2013**, *4*, 4273−4277.
(27) Jeon, I.-Y.; Choi, H.-J.; Jung, S.-M.; Seo, J.-M.; Kim, M.-J.; Dai, L.; Baek, J.-B. Large-Scale Production of Edge-Selectively Functionalized Graphene Nanoplatelets via Ball Milling and Their Use as Metal-Free Electrocatalysts for Oxygen Reduction Reaction. *J. Am. Chem. Soc.* **2013**, *135*, 1386−1393.
(28) Jeon, I.-Y.; Choi, H.-J.; Choi, M.; Seo, J.-M.; Jung, S.-M.; Kim, M.-J.; Zhang, S.; Zhang, L.; Xia, Z.; Dai, L.; Park, N.; Baek, J.-B. Facile, Scalable Synthesis of Edge-Halogenated Graphene Nanoplatelets as Efficient Metal-Free Eletrocatalysts for Oxygen Reduction Reaction. *Sci. Rep.* **2013**, *3*.
(29) Cho, D.; Lee, S.; Yang, G.; Fukushima, H.; Drzal, L. T. Dynamic Mechanical and Thermal Properties of Phenylethynyl-Terminated Polyimide Composites Reinforced with Expanded Graphite Nanoplatelets. *Macromol. Mater. Eng.* **2005**, *290*, 179−187.
(30) Wu, H.; Zhao, W.; Hu, H.; Chen, G. One-Step in Situ Ball Milling Synthesis of Polymer-Functionalized Graphene Nanocomposites. *J. Mater. Chem.* **2011**, *21*, 8626−8632.
(31) Hubert, P. J.; Kathiresan, K.; Wakabayashi, K. Filler Exfoliation and Dispersion in Polypropylene/as-Received Graphite Nanocomposites via Cryogenic Milling. *Polym. Eng. Sci.* **2011**, *51*, 2273−2281.
(32) Raza, M. A.; Westwood, A. V. K.; Brown, A. P.; Stirling, C. Composites Science and Technology. *Compos. Sci. Technol.* **2012**, *72*, 467−475.
(33) Chatterjee, S.; Wang, J. W.; Kuo, W. S.; Tai, N. H.; Salzmann, C.; Li, W. L.; Hollertz, R.; Nüesch, F. A.; Chu, B. T. T. Chemical Physics Letters. *Chem. Phys. Lett.* **2012**, *531*, 6−10.
(34) Piermattei, A.; Karthikeyan, S.; Sijbesma, R. P. Activating Catalysts with Mechanical Force. *Nature Chem.* **2009**, *1*, 133−137.
(35) Czitrom, V. One-Factor-at-a-Time Versus Designed Experiments. *American Statistician* **1999**, *53*, 126−126.
(36) Xu, X.; Khan, M. A.; Burgess, D. J. A Quality by Design (QbD) Case Study on Liposomes Containing Hydrophilic API: I. Formulation, Processing Design and Risk Assessment. *Int. J. Pharm.* **2011**, *419*, 52−59.
(37) Xu, X.; Khan, M. A.; Burgess, D. J. A Quality by Design (QbD) Case Study on Liposomes Containing Hydrophilic API: II. Screening of Critical Variables, and Establishment of Design Space at Laboratory Scale. *Int. J. Pharm.* **2012**, *423*, 543−553.
(38) Kamal, N.; Cutie, A. J.; Habib, M. J.; Zidan, A. S. QbD Approach to Investigate Product and Process Variabilities for Brain Targeting Liposomes. *J. Liposome Res.* **2014**, 1−16.
(39) Verma, S.; Lan, Y.; Gokhale, R.; Burgess, D. J. Quality by Design Approach to Understand the Process of Nanosuspension Preparation. *Int. J. Pharm.* **2009**, *377*, 185−198.
(40) Rahman, Z.; Zidan, A. S.; Khan, M. A. Non-Destructive Methods of Characterization of Risperidone Solid Lipid Nanoparticles. *Eur. J. Pharm. Biopharm.* **2010**, *76*, 127−137.
(41) Box, G. E. P.; Hunter, J. S.; Hunter, W. G. *Statistics for Experimenters: Design, Innovation, and Discovery*, 2nd ed.; John Wiley & Sons: New York, 2005.
(42) Xu, Y.; Qin, Y.; Palchoudhury, S.; Bao, Y. Water-Soluble Iron Oxide Nanoparticles with High Stability and Selective Surface Functionality. *Langmuir* **2011**, *27*, 8990−8997.
(43) Li, Y.-S.; Church, J. S.; Woodhead, A. L. Infrared and Raman Spectroscopic Studies on Iron Oxide Magnetic Nano-Particles and Their Surface Modifications. *J. Magn. Magn. Mater.* **2012**, *324*, 1543−1550.
(44) Ali-Boucetta, H.; Al-Jamal, K. T.; Kostarelos, K. Cytotoxic Assessment of Carbon Nanotube Interaction with Cell Cultures. In *Biomedical Nanotechnology*; Hurst, S. J., Ed.; Methods in Molecular Biology; Humana Press: Totowa, NJ, 2011; Vol. *726*, pp 299−312.
(45) Singh, N.; Jenkins, G. J. S.; Asadi, R.; Doak, S. H. Potential Toxicity of Superparamagnetic Iron Oxide Nanoparticles (SPION). *Nano Rev.* **2010**, *1*, 1−15.
(46) Seabra, A. B.; Paula, A. J.; de Lima, R.; Alves, O. L.; Durán, N. Nanotoxicity of Graphene and Graphene Oxide. *Chem. Res. Toxicol.* **2014**, *27*, 159−168.
(47) Gossuin, Y.; Gillis, P.; Hocq, A.; Vuong, Q. L.; Roch, A. Magnetic Resonance Relaxation Properties of Superparamagnetic Particles. *WIREs Nanomed. Nanobiotechnol.* **2009**, *1*, 299−310.
(48) Shen, J.-M.; Huang, G.; Zhou, X.; Zou, J.; Yang, Y.; Chen, Y.-F.; Men, S.-K. Safety Evaluation of Graphene Oxide-Based Magnetic Nanocomposites as MRI Contrast Agents and Drug Delivery Vehicles. *RSC Adv.* **2014**, *4*, 50464−50477.
(49) Huang, J.; Bu, L.; Xie, J.; Chen, K.; Cheng, Z.; Li, X.; Chen, X. Effects of Nanoparticle Size on Cellular Uptake and Liver MRI with Polyvinylpyrrolidone-Coated Iron Oxide Nanoparticles. *ACS Nano* **2010**, *4*, 7151−7160.
(50) Choi, J.-S.; Lee, J.-H.; Shin, T.-H.; Song, H.-T.; Kim, E. Y.; Cheon, J. Self-Confirming "and" Logic Nanoparticles for Fault-Free MRI. *J. Am. Chem. Soc.* **2010**, *132*, 11015−11017.
(51) Yu, L. X. Pharmaceutical Quality by Design: Product and Process Development, Understanding, and Control. *Pharm. Res.* **2008**, *25*, 781−791.

DOI: 10.1021/acsami.5b03577
ACS Appl. Mater. Interfaces 2015, 7, 14176−14181